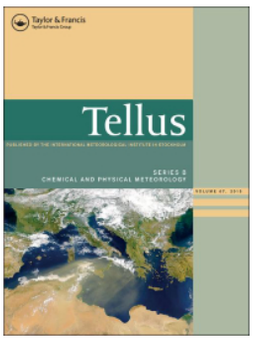

Tellus B: Chemical and Physical Meteorology

ISSN: (Print) (Online) Journal homepage: https://www.tandfonline.com/loi/zelb20

Assessment of COVID-19 effects on satellite-observed aerosol loading over China with machine learning

Hendrik Andersen, Jan Cermak, Roland Stirnberg, Julia Fuchs, Miae Kim & Eva Pauli

To cite this article: Hendrik Andersen, Jan Cermak, Roland Stirnberg, Julia Fuchs, Miae Kim & Eva Pauli (2021) Assessment of COVID-19 effects on satellite-observed aerosol loading over China with machine learning, Tellus B: Chemical and Physical Meteorology, 73:1, 1-14, DOI: 10.1080/16000889.2021.1971925

To link to this article: https://doi.org/10.1080/16000889.2021.1971925

Tellus SERIES B CHEMICAL AND PHYSICAL METEOROLOGY
PUBLISHED BY THE INTERNATIONAL METEOROLOGICAL INSTITUTE IN STOCKHOLM

Assessment of COVID-19 effects on satellite-observed aerosol loading over China with machine learning

By HENDRIK ANDERSEN[1,2]*, JAN CERMAK[1,2], ROLAND STIRNBERG[1,2], JULIA FUCHS[1,2], MIAE KIM[1,2,3], and EVA PAULI[1,2], [1]*Karlsruhe Institute of Technology (KIT), Institute of Meteorology and Climate Research, Karlsruhe, Germany;* [2]*Karlsruhe Institute of Technology (KIT), Institute of Photogrammetry and Remote Sensing, Karlsruhe, Germany;* [3]*Department of Urban & Environmental Engineering, Ulsan National Institute of Science and Technology, Ulsan, South Korea*

(Manuscript Received 24 November 2020; in final form 17 August 2021)

ABSTRACT

Aerosols are a critical component of the climate system and a risk to human health. Here, the lockdown response to the coronavirus outbreak is used to analyse effects of dramatic reduction in anthropogenic aerosol sources on satellite-retrieved aerosol optical depth (AOD). A machine learning model is applied to estimate daily AOD during the initial lockdown in China in early 2020. The model uses information on aerosol climatology, geography and meteorological conditions, and explains 69% of the day-to-day AOD variability. A comparison of model-expected and observed AOD shows that no clear, systematic decrease in AOD is apparent during the lockdown in China. During March 2020, regional AOD is observed to be significantly lower than expected by the machine learning model in some coastal regions of the North China Plains and extending to the Korean peninsula. While this may possibly indicate a small lockdown effect on regional AOD, and potentially pointing trans-boundary effects of the lockdown measures, due to uncertainties associated with the method and the limited sample sizes, this AOD decrease cannot be unequivocally attributed to reduced anthropogenic emissions. Climatologically expected AOD is compared to a weather-adjusted expectation of AOD, indicating that meteorological influences have acted to significantly increase AOD during this time, in agreement with recent literature. The findings highlight the complexity of aerosol variability and the challenges of observation-based attribution of columnar aerosol changes.

Keywords: Atmospheric aerosols, COVID-19, satellite remote sensing, machine learning

1. Introduction

Atmospheric aerosols are a key but poorly understood component of the climate system (Boucher et al., 2013), and as air pollutants also play a critical role for human health (Shiraiwa et al. 2012; Lelieveld et al. 2019). Severe air pollution episodes are a well-known problem in China, a global hotspot of aerosol abundance, and pose a major health risk to the population (e.g., Lelieveld et al. 2015; Yue et al. 2020). Also, climate-system effects of aerosols are particularly pronounced in China and over adjacent seas (Andersen et al. 2017; Hasekamp et al. 2019; Toll et al. 2019). Therefore, reaching a quantitative understanding of the potential of anthropogenic aerosol source changes on the atmospheric aerosol loading in this region is relevant for both policy makers and the climate science community.

The recent outbreak of the novel coronavirus disease 2019 (COVID-19) has affected human activities worldwide. As the initial epicentre of the outbreak, China was the first country to implement a number of unprecedented countermeasures, which caused an almost complete shutdown of public life during early 2020 (Tian et al. 2020). While Diamond and Wood (2020) and Huang et al. (2021) have reported that, dependent on the sector, only minor reductions of industrial production have taken place, the overall abrupt change in human activity (especially road traffic) has resulted in unprecedented decreases of NO_2 and to a lesser degree of particulate matter concentrations in China (Diamond and Wood 2020; Shi and Brasseur 2020; Venter et al. 2020; Tang et al. 2021; Li et al. 2021). Despite these clear reductions in

*Corresponding author. email: hendrik.andersen@kit.edu

Citation: Tellus B: 2021, 73, 1971925, 73https://doi.org/10.1080/16000889.2021.1971925

specific aerosol species, no clear signal of lockdown measures on satellite-based aerosol optical depth (AOD) has been found (Diamond and Wood 2020). This is not necessarily surprising, as NO_2 (and NO as well) is strongly driven by traffic emissions (Carslaw 2005), while AOD is influenced by many factors at once, e.g., secondary aerosol formation, aerosol natural source variability or transport, which all need to be carefully considered (detailed discussion below). Especially secondary aerosol formation has been found to have offset the reductions from reduced primary particle emission during early 2020 in China, driven by changes in atmospheric chemistry (increased oxidizing capacity related to the reduced NO_x emissions has been reported to facilitate secondary aerosol formation (Chang et al. 2020; Huang et al. 2021)) and also facilitated by the specific meteorological conditions (higher humidity, lower temperatures) during this time (Huang et al. 2021; Li et al. 2021; Tang et al. 2021). In existing studies analysing the AOD response to the lockdown, none or not all of these factors have been considered explicitly. In this context, the initial lockdown period in China provides a unique test bed to study the effects of massive but short-term reductions of anthropogenic aerosol emissions on satellite-retrieved AOD.

The attribution of aerosol changes to changes in human activity is challenging, as the variability of aerosols is very high in time and space, resulting in a low signal to noise ratio. This is because aerosol loading is not only determined by local emissions, but also by regional and long-distance transport, secondary aerosol formation, meteorological variability and terrain features (e.g., Wang et al. 2018). Indeed, Wang et al. (2020a) have simulated air pollution in China in a number of reduced-emission scenarios for the first weeks of 2020 and found that the magnitude of meteorological influences exceeded the air-pollution signal of emission reductions in China during this time. This underscores the necessity of specifically accounting for meteorological variability in order to quantify aerosol changes due to a modified source situation. This is difficult, as day-to-day aerosol variability is dependent on a number of meteorological factors at local (Tang et al. 2016; Liu et al. 2017; Zhan et al. 2017; Grange et al. 2018; Stirnberg et al. 2020) to synoptic scales (Jia et al. 2015; Ma and Guan 2018; Grange et al. 2018; Leung et al. 2018), which determine natural aerosol emissions (Scott et al. 2018), regional transport and mixing of aerosols (Cermak and Knutti 2009; Tang et al. 2016; Stirnberg et al. 2021), and secondary particle formation (Huang et al., 2014; Liu et al. 2018b; Nieminen et al., 2018; Li et al. 2019; Wang et al. 2020b; Chang et al. 2020; Ding et al. 2021; Li et al. 2021). Synoptic changes not only critically influence day-to-day variations in aerosol loading, but also explain a substantial fraction of longer-term aerosol variability, so that the meteorologically-forced variability does not necessarily cancel out over the time period of a month (Che et al. 2019). Also, while satellite-retrieved AOD is a well-validated and commonly used parameter to approximate aerosol patterns, it is affected by aerosol swelling at high humidity and in the vicinity of clouds. Both lead to an increase in AOD at a constant aerosol concentration (Quaas et al. 2010; Schwarz et al. 2017). Adding to the complexity, AOD in China features region-specific seasonal cycles (Guo et al. 2011; Luo et al. 2014; Yu et al. 2017; Ma and Guan 2018; Sogacheva et al. 2018), as well as nonlinear trends, with aerosol increases generally observed starting in the mid-1990s, but decreasing rapidly since 2013 (e.g., Zheng et al. 2018). Additionally, pollutants in China have been found to significantly vary dependent on the day of the week (Li et al. 2019). Amidst these considerations, a robust attribution of any observed AOD anomalies to changes in anthropogenic emissions is only feasible when all of these factors are controlled for at once (cf. Cermak and Knutti 2009).

The aim of the research presented here is to separate the effects of the assumed reduction in columnar aerosol loading due to the societal and economic lockdown in response to the COVID-19 situation from the natural variability, and thus to reach an attribution of columnar aerosol loading changes due to reduced anthropogenic activities during the COVID-19 period. The overarching scientific question to be answered is: Did the changes in human activity due to the lockdown measures significantly reduce AOD in China? The corresponding hypothesis to be tested is that in densely populated regions in eastern China, the observed AOD is lower than would be expected under the given meteorological conditions of the year 2020. To test this hypothesis, a state-of-the-art machine-learning technique is employed to predict AOD on the basis of a) information on local and synoptic-scale meteorological conditions, b) geographic aspects pertaining to location and topography, and c) a climatologically expected AOD that considers seasonal and weekly cycles, as well as trend information. The predicted climatologically-informed and weather-adjusted AOD expectation is compared to satellite-observed AOD, where differences are interpreted as aerosol source changes.

2. Data and methods

2.1. Data

This study focuses on a spatial domain centred on the eastern parts of China (20° N–45° N and 100° E–130° E). All data used in this study span the months of January–March in the period 2001–2020. To reduce the

Table 1. Overview of the input features used to predict log(AOD). Input features in bold are those used by the final model after recursive feature elimination.

Input feature	Time/space info	Reference
Aerosol factors (total number of features: 1)		
log(AOD_{Eclim})	instantaneous	
Meteorological factors (total number of features: 31)		
u and v wind components (10 m)	instantaneous,	(Stirnberg et al. 2020)
	24 h, 72 h average	(Cermak and Knutti 2009; Stirnberg et al. 2020)
air temperature (2 m)	instantaneous	(Megaritis et al. 2013; Stirnberg et al. 2021)
boundary layer height	instantaneous	(Petäjä et al. 2016; Tang et al. 2016; Ma and Guan 2018; Liu et al. 2018b; Stirnberg et al. 2020)
evaporation (surface)	instantaneous	
mean sea level pressure	instantaneous	(Stirnberg et al. 2020)
mean surface latent, sensible heat fluxes	instantaneous	(Tang et al. 2016)
soil (layer 1) temperature, volumetric water	instantaneous	(Scott et al. 2018; Che et al. 2019)
total columnar water vapor	instantaneous	(Boucher and Quaas 2013; Ding et al. 2021)
total precipitation	24 h	(Li et al. 2015)
temperature	BL, FT1, FT2	(Zhao et al. 2013; Petäjä et al. 2016; Ding et al. 2021; Li et al. 2021)
specific and relative humidity	BL, FT1, FT2	(Tang et al. 2016; Liu et al. 2018b; Stirnberg et al. 2018; Ding et al. 2021; Li et al. 2021)
u, v and w wind components	BL, FT1, FT2	(Ma and Guan 2018)
SHPI	instantaneous	(Jia et al. 2015)
Geographical factors (total number of features: 4)		
Surface elevation		
Latitude		
Longitude		
Land sea mask		

amount of data and computational resources needed, as well as the complexity of seasonally-dependent relationships between meteorology and aerosol loading, only the months of January, February and March (JFM) are considered.

Data on columnar aerosol loading are taken from the official product suite for the Moderate-resolution Imaging Spectroradiometer (MODIS) sensor aboard the Terra satellite. Specifically, the AOD product based on daily level 3 collection 6.1 (MOD08_D3, 'Aerosol_Optical_Depth_Land_Ocean_Mean') data are used, which features a $1^{\circ}\times1^{\circ}$ resolution (Hubanks et al. 2008; Levy et al. 2013). The data set is chosen at the spatial scale of $1^{\circ}\times1^{\circ}$ as the study is focused on regional-scale aerosol changes, because studies on climate effects of aerosols are commonly conducted at such scales (e.g., Benas et al. 2020). The authors acknowledge that by using data at this spatial resolution, local-scale characteristics, relevant especially for the assessment of local air-pollution, are not captured.

To represent meteorological factors that have been shown to influence aerosol loading, ERA5 reanalysis data from the European Centre for Medium-Range Weather Forecasts (ECMWF) are used. ERA5 is the current generation of reanalysis from the ECMWF and follow-up of ERA-Interim (Dee et al., 2011). ERA5 features hourly meteorological fields at a spatial resolution of 0.25° (Hersbach 2016). Here, meteorological fields are used at 3 UTC (close to the satellite overpass at ~11 am local time over the study domain) and resampled to fit the MODIS grid. Meteorological variables that have been found to be relevant drivers of aerosol variability by influencing natural aerosol sources, transport, chemical processes or secondary aerosol formation are chosen from the single-level and pressure-level ERA5 products, and summarized with the respective reference in Table 1. To approximate longer-term advection patterns, wind data are also used as temporal averages 24 and 72 hours before the satellite overpass. To approximate past wet scavenging of aerosol particles, total precipitation is averaged over the past 24 hours in the same manner.

As additional information on the vertical layering of the atmosphere, data on pressure levels pertaining to temperature, specific humidity, and the u, v and w

components of wind are used and averaged in three vertical layers to approximate the boundary layer (BL, all ERA5 levels between 1000 and 850 hPa), and two free tropospheric layers (FT1, all ERA5 levels between 825 and 700 hPa, and FT2, between 650 and 500 hPa).

As synoptic conditions can be difficult to capture with local meteorological information, the Siberian High position index (SHPI, Jia et al. 2015), which has been found to correlate strongly with wintertime AOD in China, is calculated. The SHPI is defined as the pressure-weighted mean of all longitudes of ERA5 grid cells exceeding 1023 hPa in a large spatial domain in the typical region of the Siberian High (60–145° E and 30–65° N). It therefore approximates the strength and location of the Siberian High, which is closely related to regionally different wintertime aerosol transport patterns to northern and southern China (Jia et al. 2015).

Along with the meteorological data, additional information on geographical factors are also taken from the reanalysis and used as predictors in the machine learning model, as terrain, coastal influences and geographic location have been shown to be important modulators of aerosol characteristics (e.g., Jia et al. 2015; Tang et al. 2016; Leung et al. 2018; Wang et al. 2018). Factors included are surface elevation, land sea mask, longitude and latitude.

2.2. Methods

A machine learning technique is used to predict an expected aerosol loading, which is then used as a comparison to satellite observed AOD. In essence, this approach uses machine learning for meteorological normalization as suggested by (Grange et al. 2018; Grange and Carslaw 2019; Petetin et al. 2020), but extends this approach by including information on geographic aspects and temporal characteristics of the time series. In this study, AOD is log-transformed for the training, testing and validation of the machine learning models. This is done as AOD is typically log-normally distributed so that its log-transformation approximates a normal distribution (e.g., Cermak and Knutti 2009). In tests conducted on the back-transformed data within this study, the training on log-transformed data has led to a slight (<5%) increase in predictive performance (higher R^2, lower RMSE) of the machine learning models used.

Gradient Boosted Regression Trees (GBRTs, (Friedman 2001; Pedregosa et al. 2011)), a state-of-the-art tree-based machine-learning model, are applied to predict log(AOD). GBRTs use an ensemble of weak learners (trees) that are sequentially added to the ensemble and fitted to its predecessor's previous residual error on the basis of gradient descent (Friedman 2001). GBRTs have been successfully applied before to study aerosol and cloud patterns and processes (Fuchs et al. 2018; Pauli et al. 2020; Stirnberg et al. 2020, 2021) and also the impact of COVID-19 on air pollution in Europe (Petetin et al. 2020). The exact architecture of the GBRTs is determined by hyperparameters (e.g., learning rate, number of trees).

A two-step modeling approach is chosen, which is illustrated in Fig. 1:

1. In the first stage, grid-cell specific GBRTs are trained to approximate the region-specific climatological signals of log(AOD) on the basis of only four input features: the year, the day of the week, the day of the year, and the number of days before/after Chinese New Year for each specific observation. This is intended to account for regional differences in a) AOD, b) its temporal cycles (Ma and Guan 2018; Sogacheva et al. 2018), and c) nonlinear trend characteristics (Zheng et al. 2018). The predicted log(AOD) can be viewed as a generalized climatological expectation at a specific point in time and space and is termed $\log(AOD_{Eclim})$. This is similar to the climatologically expected AOD used in Diamond and Wood (2020), but uses daily data instead of monthly means. To avoid overfitting of the model to the day-to-day variability, a very shallow model architecture is chosen, with only 100 trees and a maximum depth (number of decision layers in each tree) of 2. The robust Huber loss function is chosen as in Fuchs et al. (2018). With these architectural constraints, the models are only capable of a very broad estimation of patterns underlying the time series, and overfitting is not an issue. The models are not technically validated, as the goal is not to accurately predict an existing target (i.e. monthly means, which are influenced by meteorology), but rather to generalize the discussed elements of the AOD time series at each location. As such, optimizing model performance (e.g., on monthly means) would not necessarily suggest that the models generalize (e.g., trends and seasonality) well. The skill of the models to generalize the underlying temporal patterns (mainly trend and seasonality) is controlled by visualizations as shown in Fig. 2b) (and Fig. S1) for each grid box. One should note that there is not enough data to train a local model in every region separately. If the number of valid observations for the whole time period is less than 200 per grid cell (e.g., some mountainous regions in the very north west of the domain), $\log(AOD_{Eclim})$ is defined as the average log(AOD).
2. In the second stage, a single domain-wide model is used to predict daily log(AOD) on the basis of the described

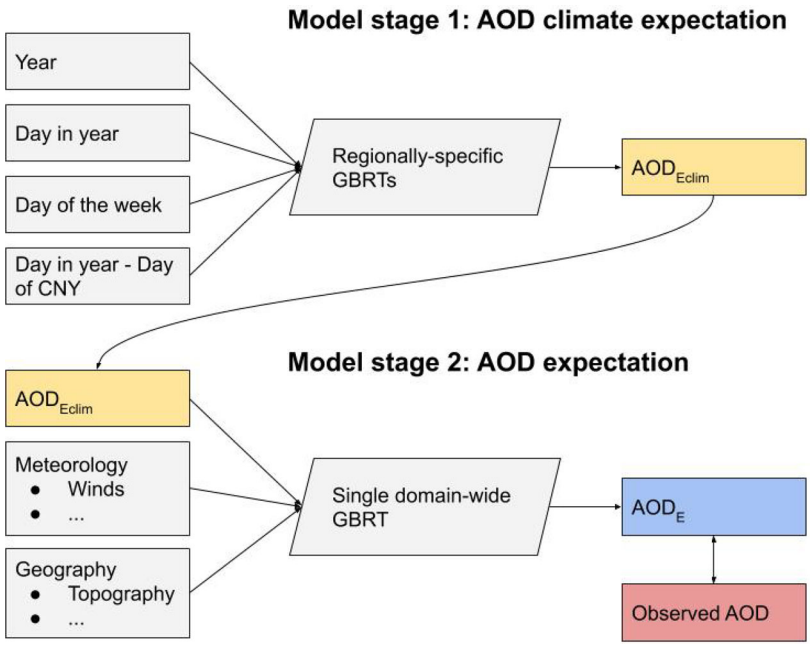

Fig. 1. Schematic overview of the two-step machine learning approach used in this study. Significant differences in the comparison of the simulated AOD_E (blue) and the observed AOD (red) during the lockdown are interpreted as aerosol source changes.

$\log(AOD_{Eclim})$, meteorological, and geographical information. As this is a much more complex task, likewise, the model architecture is more complex. The data are split up into training (67%, n = 219,033) and test (33%, n = 107,883) data sets. To evaluate potential biases or uncertainties introduced when applying the model to an unseen time period (as e.g., 2020), only data from 2001–2018 are used during training, withholding data from 2019 as an additional separate test data set. Within the training data, a recursive feature elimination is done to select only those features that are shown to be useful to predict log(AOD). This is achieved by a step-wise elimination of the least important input feature, with model skill evaluated in a 3-fold cross validation. A generic model architecture is chosen for this approach (number of trees = 5000, maximum depth = 4, all other hyperparameters at default of the scikit-learn implementation (Pedregosa et al. 2011)). The final set of features includes 36 of the original 40 features, which maximizes model skill (see Table 1; the 3 features pertaining to vertical velocity, as well as evaporation are eliminated during the feature elimination process). Based on this set of features, model hyperparameters are optimized on the training data set in a grid-search approach to determine the best combination of hyperparameters (shown in Table 2), again using 3-fold cross validation (to limit computational costs). To limit overfitting of the model, two regularization strategies are applied: 1) for each decision made by the trees during training, only a fraction of the available features are considered ($\sqrt{N_{features}}$), and 2) model training is stopped when the cross-validation score does not improve for 100 iterations (early stopping). The final set of hyperparameters is the one that performs best in the cross validation (bold numbers in Table 2). The final model performance is then tested on the completely independent test data set and on the year 2019. The predicted log(AOD) can be understood as the expected log(AOD) when meteorology, climatological context and geography are considered and is termed here as $\log(AOD_E)$. For all analyses (excluding the validation, Fig. 3a)), the results are transformed back to the original scale of AOD for clarity.

The two stage modeling architecture is chosen for two reasons: 1) To create robust region-specific climatological AOD expectations that account for nonlinear temporal characteristics of the AOD time series, and 2) to be able to have a quantitative estimate to potential weather contributions to the expected AOD (Difference between AOD_E and AOD_{Eclim}).

3. Results and discussion

Figure 2 shows results of the first modeling step to predict climatologically expected AOD_{Eclim}. In Fig. 2a), $\log(AOD_{Eclim})$ is shown as a domain average grouped by the parameter day of year. An increase in predicted

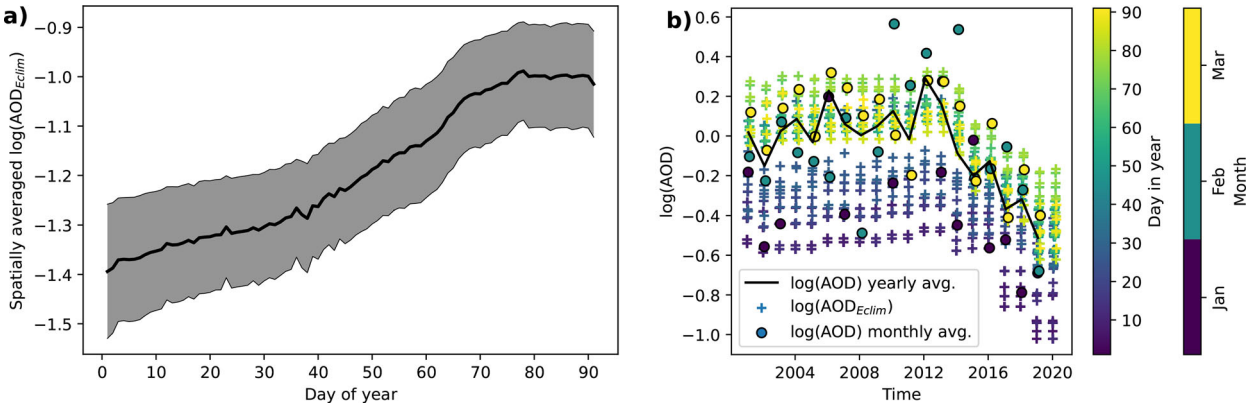

Fig. 2. Domain-average climatologically expected log(AOD$_{Eclim}$) grouped by day of year (a)), displaying seasonal characteristics of the AOD data set. The black line represents the mean, the grey area the mean ± 1 standard deviation of the regional models. Panel b) shows an example of a log(AOD$_{Eclim}$) time series for Chengdu ('+' symbol), together with long-term variability (yearly average, black), and seasonal variability (monthly average, circles) of observed log(AOD).

Table 2. Hyperparameter tuning of the GBRT model. The left-hand column names the property, and the right-hand column lists the values tested using grid search. Bold values are chosen for the final model on the basis of a 3-fold cross validation. The number of estimators is determined by early stopping as described in section 2.2, with a maximum number of estimators set to 20000.

Hyperparameter	GBRT model
Final number of estimators (trees)	**3862**
Learning rate	[**0.1**,0.03,0.01]
Maximum depth of the model	[3,4,5,**6**]
Minimum number of samples per split	[5,10,15,**20**]

log(AOD$_{Eclim}$) with day of year is apparent, also showing substantial intramonthly changes of AOD. In thorough grid-cell specific analyses, such as shown in Fig. 2b) and Fig. S1, log(AOD$_{Eclim}$) is qualitatively observed to capture well the underlying seasonal and trend patterns of AOD. One should note that AOD trends and seasonal variability are observed to differ substantially between grid cells, so that the estimated log(AOD$_{Eclim}$) patterns vary similarly. In the example shown in Fig. 2b), the seasonal pattern of AOD in the pixel closest to Chengdu is well captured by the model and combined with the long-term trend, where AOD is observed (and predicted) to rapidly decrease starting ~2012, after stricter air pollution countermeasures were introduced (Jin et al. 2016). In this example, some extremes of the monthly mean AOD are not captured (around 2012), which makes sense, as these typically are not climate signals but largely driven by meteorology, regional aerosol transport and secondary aerosol production (Huang et al., 2014; Zheng et al. 2015).

The grid-cell specific information of log(AOD$_{Eclim}$) is then forwarded to the second machine learning model where it is combined with information on meteorology and geography (see Sec. 2). On this basis, the model is applied to predict daily log(AOD) at each point in time and space. Fig. 3 provides a summary of the skill of the model to predict AOD in the study domain. The top row shows averaged spatial patterns of observed AOD (a)), predicted back-transformed AOD$_E$ (b)), and their difference (c)) in the independent test data (2001–2018). The results show that during the training period, the machine-learning model is able to reproduce the average spatial patterns well, without clear systematic regional biases. The same comparison is done for the year 2019, which was completely withheld from training, and shown in panel f). A larger absolute bias is apparent in this case, but only a very limited number of scattered pixels feature a significant difference between observed AOD and predicted AOD$_E$. This case study for 2019 acts as a guide to interpret the meaningfulness of the differences during 2020, as it shows the limitations of the method to predict in unseen years. Fig. 3d) shows the results of the validation of the day-to-day variability of log(AOD) with the independent test data set. The model is able to capture the largest part of daily log(AOD) variability (69%, 57% for back-transformed data, see Table S1). It is evident that some very low aerosol loadings are overestimated by the model (at log(AOD) < -5). This validation, however, represents a mix of spatial and temporal components of variability, as it is performed for the entire spatial domain at once. In terms of explaining day-to-day variability in each grid cell, the model performs slightly worse, with a domain average R^2 of 0.50 (0.46 for back-transformed data) but only minor spatial variation of the model's skill (Fig. 3e), standard deviation of temporal R^2: 0.15). It should be noted that skill and bias tend to vary more where less data exists for training (see Fig. 4a)). On

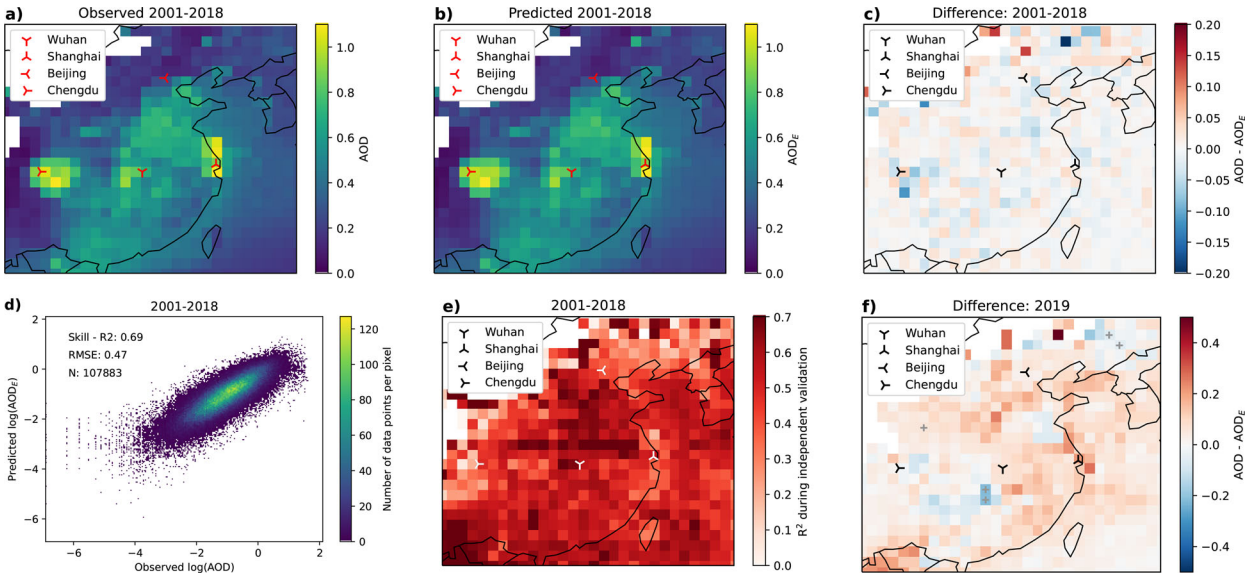

Fig. 3. Validation of the machine-learning model predicting AOD/log(AOD) with independent test data. The top row shows average observed and predicted (backtransformed) AOD of the test data in a) and b), and their difference in c) in the study domain (20° N–45° N and 100° E–130° E). Panel d) shows a scatter plot summarizing the model skill to predict log(AOD) over the entire domain and therefore represents a combination of spatial and temporal skill. e) Spatial patterns of model skill in predicting the temporal variability of log(AOD) in each grid cell (R^2). Panel f) shows the difference between observed AOD and predicted (back-transformed) AOD_E, with grey '+' symbols showing significance at 0.01 level of an independent two-sided t test.

this basis, model predictions are used as comparison to the observed AOD in early 2020 to attribute anomalies to COVID-19 lockdown-induced emission changes.

In Fig. 5a), differences between observed AOD and predicted AOD_E for all of JFM 2020 are shown. Since the influences of seasonality, trends, and meteorological conditions are inherent in AOD_E, differences to observed AOD can be interpreted as differences in aerosol emissions under consideration of the limitations of the method (see Fig. 3). No clear, systematic differences between observed AOD and AOD_E as hypothesized are evident. In the North China Plains, predicted AOD_E tends to be higher than observed AOD, but this difference is only significant in some pixels. In light of the limitations of the method illustrated by the test results for the year of 2019, it is thus hard to attribute these differences to decreased anthropogenic emissions during the lockdown. These results agree well with findings from Diamond and Wood (2020) who also analysed level 3 MODIS AOD at a 1° x1° resolution, but used monthly averages without explicitly controlling for meteorological variability. In some regions, the observed AOD is actually significantly higher than AOD_E, contrary to the hypothesis of this study. The clearest of these patterns is in the regions of northern Hebei north of Beijing and Liaoning. Here, dust transport from the Kumutage and Taklamakan deserts is a frequent phenomenon (Tang et al. 2016; Yu et al. 2017), which increases the variability of AOD in this region during winter. While some of the AOD variability related to dust transport should be explained by the model, certainly some limitations to modeling dust transport exist in the current modeling framework. For example, the model has no information on meteorology that controls emissions at the source region (e.g., previous precipitation, soil moisture and winds; Che et al. 2019). Including this information is difficult, as source regions vary, and the transport time and trajectory from source region to the receptor region depend on the synoptic situation controlling the transport. Also, wet scavenging along the trajectory is likely to be a factor limiting the model's capability to predict such situations. Observed AOD also significantly exceeds AOD_E in south-western parts of the domain, in vicinity to the borders to Vietnam and Laos. These positive AOD anomalies are likely caused by the extraordinary number of wildfires occurring in the southeastern Asian Peninsula during February and March 2020 (Jenner 2020). Such AOD anomalies due to wildfire emissions could only be explained by a machine learning model if they also would occur in a similar way in the training data and were captured by the input features, which is not the case here.

Differences between observed AOD and AOD_E are analysed for the months of January, February and March (the lockdown in Wuhan started at the end of January (Zhu et al. 2020)) to further investigate the temporal evolution of differences between AOD and AOD_E during

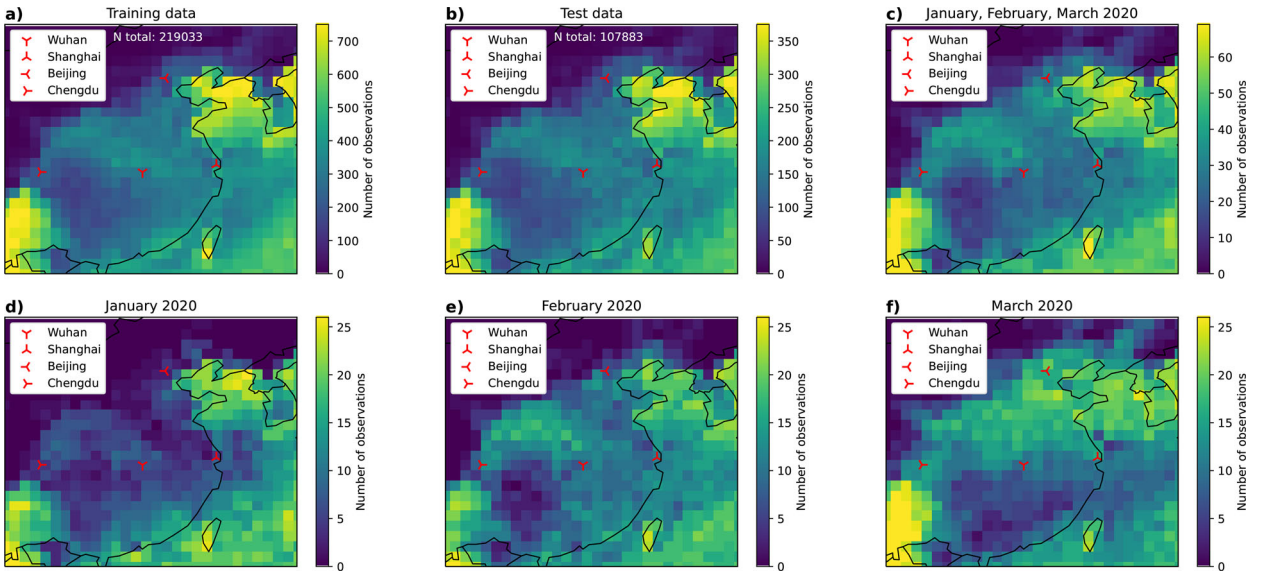

Fig. 4. Number of valid AOD observations during a) training, b) testing, c) JFM 2020, d) January 2020, e) February 2020, and f) March 2020 in the study domain (20° N–45° N and 100° E–130° E).

this period. In January (Fig. 5b)), observed AOD is higher than predicted AOD_E throughout the North China Plains, however, this difference is based on only very few data points (Fig. 4d)) and hence is not significant in most regions. While this pattern should not be over-interpreted, the very low number of samples indicates a prevalence of clouds in this region during this time, and the positive differences could be related to aerosol swelling or cloud-related processes that are not captured by the model. There is a region where observed AOD is significantly higher than predicted AOD_E in the province of Guizhou in the southwestern parts of the domain. However, as this is one of the more rural and less densely population regions in China, and first lockdown measures were put in place at the end of January in Wuhan, these cannot be interpreted as related to the lockdown-related changes in anthropogenic emissions. These differences rather underscore the difficulty in the interpretation of the results. During February (Fig. 5c)), differences between AOD and AOD_E are similar to those found for the JFM period. It should be noted that the spatial patterns of the differences in February closely match the findings from Diamond and Wood (2020), underscoring that the patterns apparent in Fig. 5 are unlikely to be artefacts created by the machine-learning model. In March 2020 (Fig. 5d)), observed AOD is again lower than predicted AOD_E in the North China Plains, however, in most regions this difference is not significant (p values > 0.01). This pattern extends over the adjacent Yellow Sea and to the Korean peninsula, where differences are observed to be significant. One should note though that the significance measure of the t test is affected by the higher number of samples over the Yellow Sea rather than the difference between AOD and AOD_E being larger. With sample sizes varying this much over the considered time and region using daily observations and therefore including this information instead of monthly average data are thus advantageous for such analyses.

To more closely evaluate this AOD anomaly from the expected AOD_E in the North China Plains and the adjacent Yellow Sea, Fig. 6 shows distributions of observed AOD, and predicted AOD_E and AOD_{Eclim} for the test data (2001–2018, a)) and March 2020 (b)). It is apparent that during the test period, the median prediction of AOD_E and AOD_{Eclim} is close to the observations, but that only AOD_E captures the variability of observed AOD. This is expected, as AOD_{Eclim} is purely a climatological expectation without considering potential weather influences. During March 2020, AOD_{Eclim} is lower than during the test period, reflecting the decreasing trend in aerosol loadings in this region. While the observed AOD is lower than this climatological expectation, the weather adjusted AOD_E is actually higher than AOD_{Eclim}. It is thus noteworthy that during February and March 2020, AOD was lower than expected in the North China Plains, and may possibly be related to the lockdown measures, and potentially pointing trans-boundary effects of the lockdown measures. In light of the uncertainties associated with the method, though, these AOD reductions cannot be unequivocally be attributed to reduced anthropogenic emissions. The results do show that

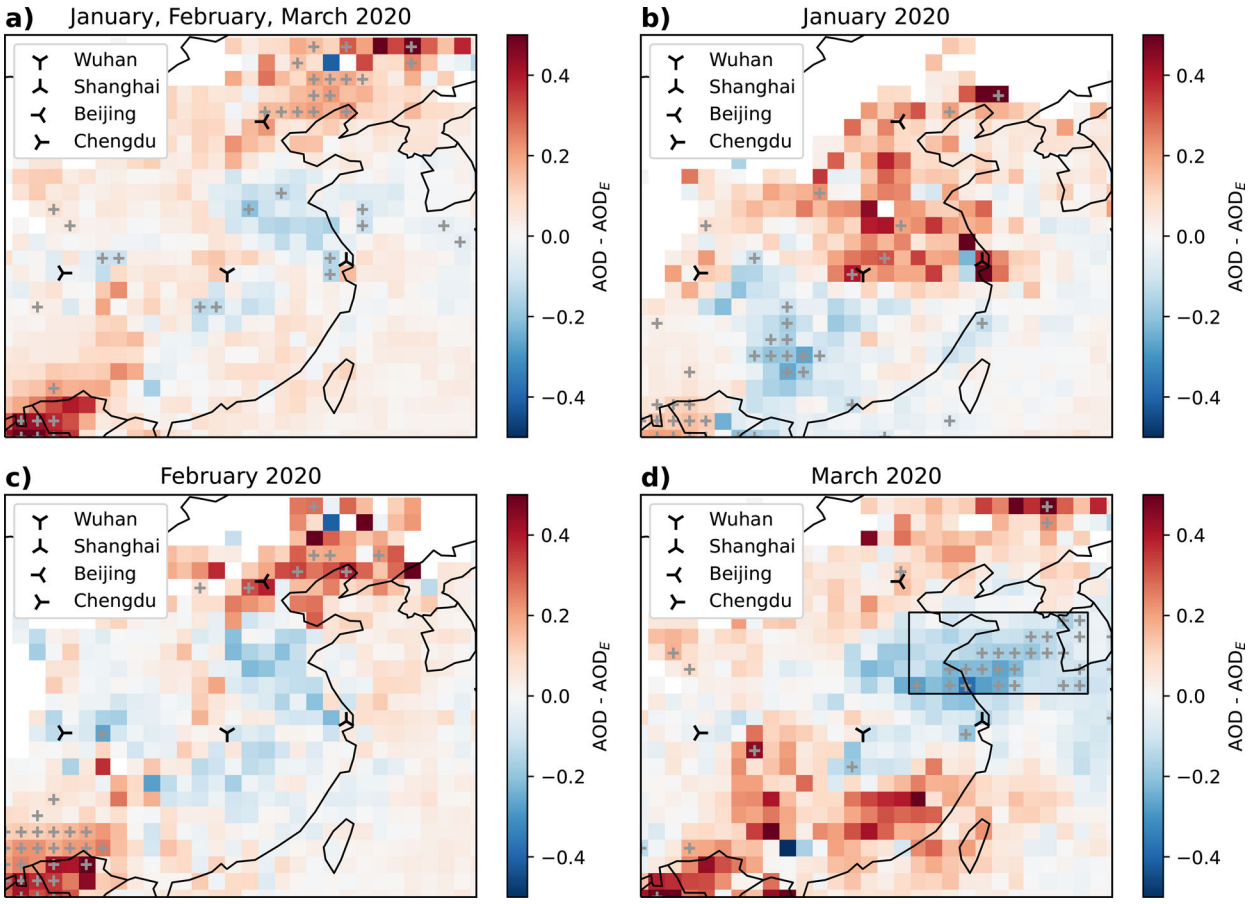

Fig. 5. Comparison of observed AOD 2020 minus AOD$_E$ for a) JFM 2020, b) January 2020, c) February 2020, and d) March 2020 in the study domain (20° N–45° N and 100° E–130° E). Grey '+' symbols show significance at 0.01 level of an independent two-sided t test. The black box in panel d) shows the region that is further investigated in Fig. 6.

meteorological factors need to be explicitly considered in such analyses, as expected meteorological influences may otherwise partially mask the AOD changes. It should be noted that passive sensor AOD is an integrated columnar observation, which means that changes in the vertical distribution of aerosols cannot be detected. In a recent study using ground-based polarization lidar measurements over Wuhan, Yin et al. (2021) separated the AOD contributions of boundary layer and free-tropospheric aerosols to total AOD and found that during the lockdown, boundary layer AOD was reduced while free-tropospheric AOD was increased and actually dominated the total AOD signal, which is a clear anomaly in the time series. This indicates that some of the lockdown-related aerosol loading signals may not be detectable using column-integrated AOD observations.

Spatial patterns of the differences between climatologically expected AOD$_{Eclim}$ and AOD$_E$ during JFM 2020 are shown in Fig. 7. It is apparent that AOD$_E$ is significantly higher than AOD$_{Eclim}$ for the entire region of the North China Plains and a large region centered around Chengdu. This suggests that meteorological influences have led to a higher model expectation of AOD$_E$, underscoring the necessity of controlling for meteorological influences rather than using monthly average data in such analyses. This result is in agreement with recent studies that show that during the initial lockdown in China, increased secondary aerosol production was facilitated by high humidity and low air temperatures and changes in atmospheric chemistry (Huang et al. 2021; Li et al. 2021; Tang et al. 2021), and thus acted to increase the column aerosol loading during this time. One should note that while secondary aerosol production can be modified by meteorological conditions (e.g., Liu et al. 2018b), it also critically depends on the abundance of gaseous precursors (e.g., Liu et al. 2018a). The planetary boundary layer height was observed to have been abnormally low in northern China during the lockdown, which has been linked to strong haze conditions (Su et al. 2020). The results also support Wang et al. (2020a) whose numerical

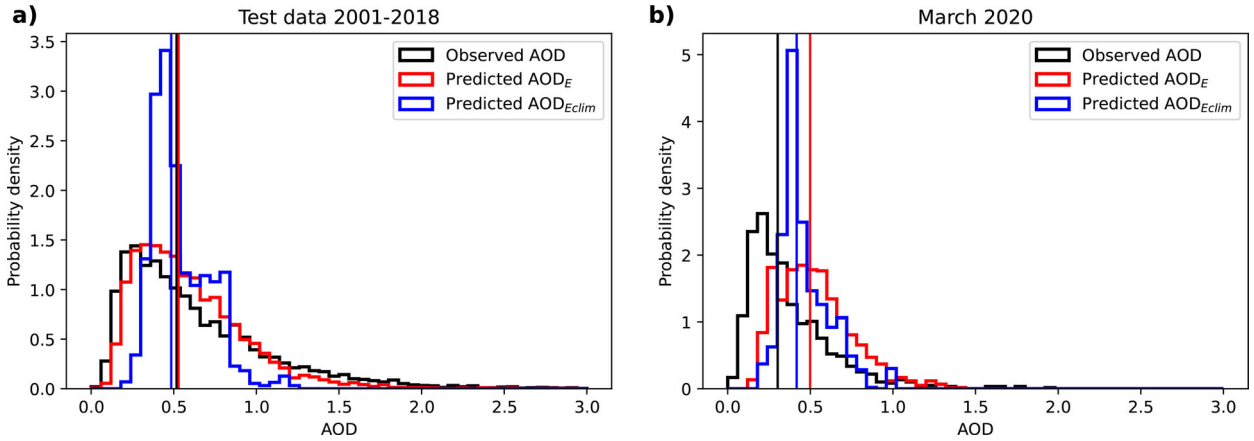

Fig. 6. Comparison of observed AOD and predicted AOD_E and AOD_{Eclim} distributions of the region shown as a box in Fig. 5d) for test data in the time period of 2001–2018 (a)), and March 2020 (b)). Predicted log(AOD_E) and log(AOD_{Eclim}) are back-transformed for the comparison. Thin vertical lines shows the median of the distributions.

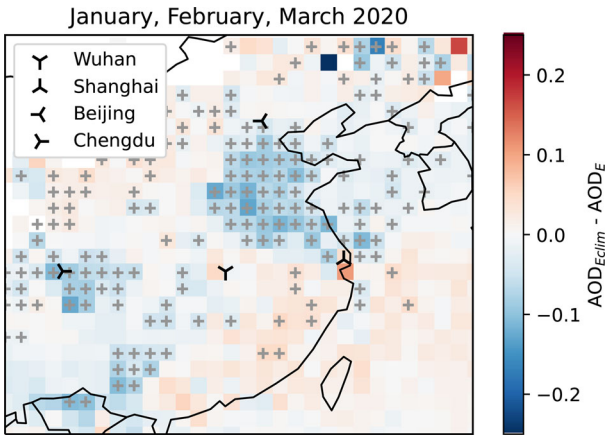

Fig. 7. Comparison of climatologically expected AOD_{Eclim} minus AOD_E for JFM 2020 in the study domain (20° N–45° N and 100° E–130° E), grey '+' symbols show significance at 0.01 level of an independent two-sided t test.

modelling results showed that the magnitude of meteorological influences exceeded the air-pollution signal of emission reductions during the lockdown period in China. While the differences between AOD_{Eclim} and AOD_E are not as large as the differences between observed AOD and AOD_E, they are not as affected by limited sampling (prediction every day, n = 90) and show a clear and spatially coherent structure.

4. Conclusions

In this study, a machine-learning model is applied to predict satellite-observed AOD on the basis of climatologically expected AOD, meteorological factors and geographical information to attribute AOD anomalies to reduced anthropogenic emissions during the COVID-19 period in China. The model is shown to be capable of well representing daily AOD variability in an independent test data set (spatiotemporal R^2: 0.69, domain-average temporal R^2: 0.50), with no systematic bias. In a separate test conducted on a year that is completely withheld from training (2019), the bias is higher, showing some limitations of the model to predict for an unseen time period. The main findings of comparisons between observed AOD and predicted AOD_E are that:

- No clear, systematic reduction of AOD with respect to the model expectation is found that can unequivocally be attributed to reduced anthropogenic emissions during the COVID-19 period.
- Observed AOD is lower than expected over the North China Plain during February and March, but in most regions these differences are not significant. In March 2020, this pattern extends over the Yellow Sea and to the Korean Peninsula, where differences are frequently observed to be significant at the 0.01 level. While this finding is noteworthy, in light of the uncertainties related to the method and the limited number of samples, these are not interpreted as a clearly evidential signature of reduced anthropogenic emissions during the COVID-19 period.
- Climatologically expected AOD_{Eclim} is compared to the weather-adjusted expectation (AOD_E) for the months of January, February and March. It is found that AOD_E is significantly higher than AOD_{Eclim} for the region of the North China Plains and a region centered around Chengdu. This suggests that meteorological influences have acted to increase AOD during this time, in agreement with recent literature.
- AOD_E significantly underestimates AOD in northern and southern parts of China, likely due to processes

that are not captured by the machine-learning model as e.g., likely wildfire emissions (southern China), aerosol swelling, meteorological influences or secondary aerosol production.

The findings suggest that extensive anthropogenic aerosol source reductions (e.g., air-pollution measures) does not necessarily lead to a detectable reduction in satellite retrieved regional columnar aerosol loadings. The findings also highlight the complexity of columnar aerosol variability in a large spatial domain and underscore the challenge of detecting changes in column aerosol loading due to changes in anthropogenic activity and the necessity to account for meteorological influences.

Acknowledgements

We thank two anonymous reviewers for their careful reviews which have helped improve the manuscript.

Disclosure statement

The authors declare that they have no conflict of interest.

Funding

EP is funded by the Graduate Funding from the German States. We acknowledge the support by the European Commission, H2020 Research Infrastructures (FORCeS (grant no. 821205)), and the support by the Publication Fund of the Karlsruhe Institute of Technology (KIT).

Code and data availability

The ERA5 meteorological reanalysis data are freely available at the Copernicus Climate Change Service (C3S) Climate Date Store: https://cds.climate.copernicus.eu/#!/search?text = ERA5&type = dataset (last access: April 27th, 2020). MODIS data are freely available at the Level-1 and Atmosphere Archive & Distribution System (LAADS) Distributed Active Archive Center (DAAC): https://ladsweb.modaps.eosdis.nasa.gov/archive/allData/61/MOD08/_D3/ (last access: April 10th, 2020). Code for data processing and modeling is available from the corresponding author upon reasonable request.

Author contributions

HA and JC had the idea for the analysis. HA obtained and analysed most of the data sets, conducted the original research and wrote the manuscript. EP and MK helped with the development of the machine learning model. All authors contributed to study design, manuscript preparation, and the interpretation of findings.

Supplementary material

Supplemental data for this article can be accessed online at https://doi.org/10.1080/16000889.2021.1971925.

References

Andersen, H., Cermak, J., Fuchs, J., Knutti, R. and Lohmann, U. 2017. Understanding the drivers of marine liquid-water cloud occurrence and properties with global observations using neural networks. *Atmos. Chem. Phys.* **17**, 9535–9546. doi:10.5194/acp-17-9535-2017

Benas, N., Fokke Meirink, J., Karlsson, K. G., Stengel, M. and Stammes, P. 2020. Satellite observations of aerosols and clouds over southern China from 2006 to 2015: Analysis of changes and possible interaction mechanisms. *Atmos. Chem. Phys.* **20**, 457–474. doi:10.5194/acp-20-457-2020

Boucher, O. and Quaas, J. 2013. Water vapour affects both rain and aerosol optical depth. *Nature Geosci.* **6**, 4–5. doi:10.1038/ngeo1692

Boucher, O., Randall, D., Artaxo, P., Bretherton, C., Feingold, G. and co-authors. 2013. (). Clouds and Aerosols. In *Climate Change 2013: The Physical Science Basis, Contribution of Working Group I to the Fourth Assessment Report of the Intergovernmental Panel on Climate Change*. (eds. T.F. Stocker, D. Qin, G.K. Plattner, M. Tignor, S.K. Allen, J. Boschung, A. Nauels, Y. Xia, V. Bex, and P.M. Midgley,). Cambridge University Press, Cambridge, UK.

Carslaw, D. C. 2005. Evidence of an increasing NO2/NOX emissions ratio from road traffic emissions. *Atmos. Environ.* **39**, 4793–4802. doi:10.1016/j.atmosenv.2005.06.023

Cermak, J. and Knutti, R. 2009. Beijing olympics as an aerosol field experiment. *Geophys. Res. Lett.* **36**, L10806. doi:10.1029/2009GL038572

Chang, Y., Huang, R. J., Ge, X., Huang, X., Hu, J. and co-authors. 2020. Puzzling haze events in china during the coronavirus (COVID-19) shutdown. *Geophys. Res. Lett.* **47**, 1–11.

Che, H., Gui, K., Xia, X., Wang, Y., Holben, B. N. and co-authors. 2019. Large contribution of meteorological factors to inter-decadal changes in regional aerosol optical depth. *Atmos. Chem. Phys.* **19**, 10497–10523. doi:10.5194/acp-19-10497-2019

Dee, D. P., Uppala, S. M., Simmons, A. J., Berrisford, P., Poli, P. and co-authors. 2011. The ERA-Interim reanalysis: configuration and performance of the data assimilation system. *QJR. Meteorol. Soc.* **137**, 553–597. doi:10.1002/qj.828

Diamond, M. S. and Wood, R. 2020. Limited regional aerosol and cloud microphysical changes despite unprecedented decline in nitrogen oxide pollution during the February 2020 COVID-19 shutdown in China. *Geophys Res Lett*. **47**, e2020GL088913. doi:10.1029/2020GL088913.

Ding, J., Dai, Q., Zhang, Y., Xu, J., Huangfu, Y. and co-authors. 2021. Air humidity affects secondary aerosol

formation in different pathways. *Sci. Total Environ.* **759**, 143540. doi:10.1016/j.scitotenv.2020.143540

Friedman, J. H. 2001. Greedy function approximation: A gradient boosting machine. *Annals of Statistics* **29**, 1189–1232.

Fuchs, J., Cermak, J. and Andersen, H. 2018. Building a cloud in the Southeast Atlantic: Understanding low-cloud controls based on satellite observations with machine learning. *Atmos. Chem. Phys.* **18**, 16537–16552. doi:10.5194/acp-18-16537-2018

Grange, S. K. and Carslaw, D. C. 2019. Using meteorological normalisation to detect interventions in air quality time series. *Sci. Total Environ.* **653**, 578–588. doi:10.1016/j.scitotenv.2018.10.344

Grange, S. K., Carslaw, D. C., Lewis, A. C., Boleti, E. and Hueglin, C. 2018. Random forest meteorological normalisation models for Swiss PM10 trend analysis. *Atmos. Chem. Phys.* **18**, 6223–6239. doi:10.5194/acp-18-6223-2018

Guo, J. P., Zhang, X. Y., Wu, Y. R., Zhaxi, Y., Che, H. Z. and co-authors. 2011. Spatio-temporal variation trends of satellite-based aerosol optical depth in China during 1980-2008. *Atmos. Environ.* **45**, 6802–6811. doi:10.1016/j.atmosenv.2011.03.068

Hasekamp, O. P., Gryspeerdt, E. and Quaas, J. 2019. Analysis of polarimetric satellite measurements suggests stronger cooling due to aerosol-cloud interactions. *Nat. Commun.* **2**, 1–7.

Hersbach, H. (2016.). The ERA5 atmospheric reanalysis. *AGU Fall Meeting Abstracts*.

Huang, R. J., Zhang, Y., Bozzetti, C., Ho, K. F., Cao, J. J. and co-authors. 2014. High secondary aerosol contribution to particulate pollution during haze events in China. *Nature* **514**, 218–222. doi:10.1038/nature13774

Huang, X., Ding, A., Gao, J., Zheng, B., Zhou, D. and co-authors. 2021. Enhanced secondary pollution offset reduction of primary emissions during COVID-19 lockdown in China. *National Science Review* **8**, https://academic.oup.com/nsr/article/8/2/nwaa137/5859289.

Hubanks, P. A., King, M. D., Platnick, S. and Pincus, R. (2008.). MODIS Atmosphere L3 Gridded Product Algorithm Theoretical Basis Document No. ATBD-MOD-30 for Level-3 Global Gridded Atmosphere Products (08_D3, 08_E3, 08_M3).

Jenner, L. 2020. Southeast Asian peninsula displays large concentrations of fires. https://www.nasa.gov/image-feature/goddard/2020/southeast-asian-peninsula-displays-large-concentrations-of-fires.

Jia, B., Wang, Y., Yao, Y. and Xie, Y. 2015. A new indicator on the impact of large-scale circulation on wintertime particulate matter pollution over China. *Atmos. Chem. Phys.* **15**, 11919–11929. doi:10.5194/acp-15-11919-2015

Jin, Y., Andersson, H. and Zhang, S. 2016. Air pollution control policies in China: A retrospective and prospects. *Int. J. Environ. Res. Public Health* **13**, 1219.

Lelieveld, J., Evans, J. S., Fnais, M., Giannadaki, D. and Pozzer, A. 2015. The contribution of outdoor air pollution sources to premature mortality on a global scale. *Nature* **525**, 367–371. doi:10.1038/nature15371

Lelieveld, J., Klingmüller, K., Pozzer, A., Burnett, R. T., Haines, A. and co-authors. 2019. Effects of fossil fuel and total anthropogenic emission removal on public health and climate. *Proc. Natl. Acad. Sci. USA.* **116**, 7192–7197. doi:10.1073/pnas.1819989116

Leung, D. M., Tai, A. P., Mickley, L. J., Moch, J. M., Van Donkelaar, A. and co-authors. 2018. Synoptic meteorological modes of variability for fine particulate matter (PM2.5) air quality in major metropolitan regions of China. *Atmos. Chem. Phys.* **18**, 6733–6748. doi:10.5194/acp-18-6733-2018

Levy, R. C., Mattoo, S., Munchak, L. A., Remer, L. A., Sayer, A. M. and co-authors. 2013. The Collection 6 MODIS aerosol products over land and ocean. *Atmos. Meas. Tech.* **6**, 2989–3034. doi:10.5194/amt-6-2989-2013

Li, R., Wang, Z., Cui, L., Fu, H., Zhang, L. and co-authors. 2019. Air pollution characteristics in China during 2015-2016: Spatiotemporal variations and key meteorological factors. *Sci. Total. Environ.* **648**, 902–915. doi:10.1016/j.scitotenv.2018.08.181

Li, R., Zhao, Y., Fu, H., Chen, J., Peng, M. and co-authors. 2021. Substantial changes of gaseous pollutants and chemical compositions in fine particles in North China Plain during COVID-19 lockdown period: anthropogenic vs meteorological influences. *Atmos. Chem. Phys.* **21**, 8677–8692. doi:10.5194/acp-21-8677-2021

Li, Y., Chen, Q., Zhao, H., Wang, L. and Tao, R. 2015. Variations in pm10, pm2.5 and pm1.0 in an urban area of the sichuan basin and their relation to meteorological factors. *Atmosphere* **6**, 150–163. doi:10.3390/atmos6010150

Liu, J., Chu, B., Chen, T., Liu, C., Wang, L. and co-authors. 2018a. Secondary organic aerosol formation from ambient air at an urban site in Beijing: effects of OH exposure and precursor concentrations. *Environ. Sci. Technol.* **52**, 6834–6841. doi:10.1021/acs.est.7b05701

Liu, Q., Jia, X., Quan, J., Li, J., Li, X. and co-authors. 2018b. New positive feedback mechanism between boundary layer meteorology and secondary aerosol formation during severe haze events. *Sci. Rep.* **8**, 6095–6098. doi:10.1038/s41598-018-24366-3

Liu, T., Gong, S., He, J., Yu, M., Wang, Q. and co-authors. 2017. Attributions of meteorological and emission factors to the 2015 winter severe haze pollution episodes in China's Jing-Jin-Ji area. *Atmos. Chem. Phys.* **17**, 2971–2980. doi:10.5194/acp-17-2971-2017

Luo, Y., Zheng, X., Zhao, T. and Chen, J. 2014. A climatology of aerosol optical depth over China from recent 10years of MODIS remote sensing data. *Int. J. Climatol.* **34**, 863–870. doi:10.1002/joc.3728

Ma, F. and Guan, Z. 2018. Seasonal variations of aerosol optical depth over east China and India in relationship to the Asian monsoon circulation. *J. Meteorol. Res.* **32**, 648–660. doi:10.1007/s13351-018-7171-1

Megaritis, A. G., Fountoukis, C., Charalampidis, P. E., Pilinis, C. and Pandis, S. N. 2013. Response of fine particulate matter concentrations to changes of emissions and temperature in Europe. *Atmos. Chem. Phys.* **13**, 3423–3443. doi:10.5194/acp-13-3423-2013

Nieminen, T., Kerminen, V.-M., Petäjä, T., Aalto, P. P., Arshinov, M. and co-authors. 2018. Global analysis of continental boundary layer new particle formation based on long-term measurements. *Atmos. Chem. Phys.* **18**, 14737–14756. doi:10.5194/acp-18-14737-2018

Pauli, E., Andersen, H., Bendix, J., Cermak, J. and Egli, S. 2020. Determinants of fog and low stratus occurrence in continental central Europe – a quantitative satellite-based evaluation. *J. Hydrol.* **591**, 125451. doi:10.1016/j.jhydrol.2020.125451

Pedregosa, F., Varoquaux, G., Gramfort, A., Michel, V., Thirion, B. and co-authors. 2011. Scikit-learn: Machine Learning in Python. *J. Mach. Learn. Res.* **12**, 2825–2830.

Petäjä, T., Järvi, L., Kerminen, V. M., Ding, A. J., Sun, J. N. and co-authors. 2016. Enhanced air pollution via aerosol-boundary layer feedback in China. *Sci. Rep.* **6**, 1–6.

Petetin, H., Bowdalo, D., Soret, A., Guevara, M., Jorba, O. and co-authors. 2020. Meteorology-normalized impact of the COVID-19 lockdown upon NO2 pollution in Spain. *Atmos. Chem. Phys.* **20**, 11119–11141. doi:10.5194/acp-20-11119-2020

Quaas, J., Stevens, B., Stier, P. and Lohmann, U. 2010. Interpreting the cloud cover - aerosol optical depth relationship found in satellite data using a general circulation model. *Atmos. Chem. Phys.* **10**, 6129–6135. doi:10.5194/acp-10-6129-2010

Schwarz, K., Cermak, J., Fuchs, J. and Andersen, H. 2017. Mapping the twilight zone—what we are missing between clouds and aerosols. *Remote Sens.* **9**, 577. doi:10.3390/rs9060577

Scott, C. E., Arnold, S. R., Monks, S. A., Asmi, A., Paasonen, P. and co-authors. 2018. Substantial large-scale feedbacks between natural aerosols and climate. *Nature Geosci.* **11**, 44–48. doi:10.1038/s41561-017-0020-5

Shi, X. and Brasseur, G. P. 2020. The Response in Air Quality to the Reduction of Chinese Economic Activities During the COVID-19 Outbreak. *Geophys. Res. Lett.* **47**, e2020GL088070–e2020GL088078.

Shiraiwa, M., Selzle, K. and Pöschl, U. 2012. Hazardous components and health effects of atmospheric aerosol particles: Reactive oxygen species, soot, polycyclic aromatic compounds and allergenic proteins. *Free Radic. Res.* **46**, 927–939. doi:10.3109/10715762.2012.663084

Sogacheva, L., Rodriguez, E., Kolmonen, P., Virtanen, T. H., Saponaro, G. and co-authors. 2018. Spatial and seasonal variations of aerosols over China from two decades of multi-satellite observations - Part 2: AOD time series for 1995-2017 combined from ATSR ADV and MODIS C6.1 and AOD tendency estimations. *Atmos. Chem. Phys.* **18**, 16631–16652. doi:10.5194/acp-18-16631-2018

Stirnberg, R., Cermak, J. and Andersen, H. 2018. An analysis of factors influencing the relationship between satellite-derived AOD and ground-level PM10. *Remote Sens.* **10**, 1353. doi:10.3390/rs10091353

Stirnberg, R., Cermak, J., Fuchs, J. and Andersen, H. 2020. Mapping and understanding patterns of air quality using satellite data and machine learning. *J. Geophys. Res. Atmos.* **125**, e2019JD031380.

Stirnberg, R., Cermak, J., Kotthaus, S., Haeffelin, M., Andersen, H. and co-authors. 2021. Meteorology-driven variability of air pollution (PM1) revealed with explainable machine learning. *Atmos. Chem. Phys.* **21**, 3919–3948. doi:10.5194/acp-21-3919-2021

Su, T., Li, Z., Zheng, Y., Luan, Q. and Guo, J. 2020. Abnormally shallow boundary layer associated with severe air pollution during the COVID-19 lockdown in China. *Geophys. Res. Lett.* **47**, e2020GL090041.

Tang, G., Zhang, J., Zhu, X., Song, T., Münkel, C. and co-authors. 2016. Mixing layer height and its implications for air pollution over Beijing, China. *Atmos. Chem. Phys.* **16**, 2459–2475. doi:10.5194/acp-16-2459-2016

Tang, L., Shang, D., Fang, X., Wu, Z., Qiu, Y. and co-authors. 2021. More Significant Impacts From New Particle Formation on Haze Formation During COVID-19 Lockdown. *Geophys. Res. Lett.* **48**, e2020GL091591.

Tian, H., Liu, Y., Li, Y., Wu, C. H., Chen, B. and co-authors. 2020. An investigation of transmission control measures during the first 50 days of the COVID-19 epidemic in China. *Science* **368**, 638–642. doi:10.1126/science.abb6105

Toll, V., Christensen, M., Quaas, J. and Bellouin, N. 2019. Weak average liquid-cloud-water response to anthropogenic aerosols. *Nature* **572**, 51–55. doi:10.1038/s41586-019-1423-9

Venter, Z. S., Aunan, K., Chowdhury, S. and Lelieveld, J. 2020. COVID-19 lockdowns cause global air pollution declines with implications for public health risk. medRxiv 5, 2020.04.10.20060673.

Wang, P., Chen, K., Zhu, S., Wang, P. and Zhang, H. 2020a. Severe air pollution events not avoided by reduced anthropogenic activities during COVID-19 outbreak. *Resour. Conserv. Recycl.* **158**, 104814. doi:10.1016/j.resconrec.2020.104814

Wang, T., Huang, X., Wang, Z., Liu, Y., Zhou, D. and co-authors. 2020b. Secondary aerosol formation and its linkage with synoptic conditions during winter haze pollution over eastern china. *Sci. Total Environ.* **730**, 138888. doi:10.1016/j.scitotenv.2020.138888

Wang, X., Dickinson, R. R. E., Su, L., Zhou, C. and Wang, K. 2018. PM2.5 pollution in China and how it has been exacerbated by terrain and meteorological conditions. *Bull. Am. Meteorol. Soc.* **99**, 105–120. doi:10.1175/BAMS-D-16-0301.1

Yin, Z., Yi, F., Liu, F., He, Y., Zhang, Y. and co-authors. 2021. Long-term variations of aerosol optical properties over wuhan with polarization lidar. *Atmos. Environ.* **259**, 118508. doi:10.1016/j.atmosenv.2021.118508

Yu, X., Lü, R., Liu, C., Yuan, L., Shao, Y. and co-authors. 2017. Seasonal variation of columnar aerosol optical properties and radiative forcing over Beijing, China. *Atmos. Environ.* **166**, 340–350. doi:10.1016/j.atmosenv.2017.07.011

Yue, H., He, C., Huang, Q., Yin, D. and Bryan, B. A. 2020. Stronger policy required to substantially reduce deaths from PM2.5 pollution in China. *Nat. Commun.* **11**, 1462–1410. doi:10.1038/s41467-020-15319-4

Zhan, D., Kwan, M. P., Zhang, W., Wang, S. and Yu, J. 2017. Spatiotemporal variations and driving factors of air pollution in China. *Int. J. Environ. Res. Public Health* **14**, 1–18.

Zhao, X. J., Zhao, P. S., Xu, J., Meng, W., Pu, W. W. and co-authors. 2013. Analysis of a winter regional haze event and its formation mechanism in the North China Plain. *Atmos. Chem. Phys. Discuss.* **13**, 903–933.

Zheng, B., Tong, D., Li, M., Liu, F., Hong, C. and co-authors. 2018. Trends in China's anthropogenic emissions since 2010

as the consequence of clean air actions. *Atmos. Chem. Phys.* **18**, 14095–14111. doi:10.5194/acp-18-14095-2018

Zheng, G. J., Duan, F. K., Su, H., Ma, Y. L., Cheng, Y. and co-authors. 2015. Exploring the severe winter haze in Beijing: The impact of synoptic weather, regional transport and heterogeneous reactions. *Atmos. Chem. Phys.* **15**, 2969–2983. doi:10.5194/acp-15-2969-2015

Zhu, Y., Xie, J., Huang, F. and Cao, L. 2020. Association between short-term exposure to air pollution and COVID-19 infection: Evidence from China. *Sci. Total Environ.* **727**, 138704.